JOURNAL OF MATERIALS SCIENCE 9 (1974) 41–56

Direct observation of grain-boundary dislocations in the FeCo alloy

Part 2 *Transmission electron microscopy observations*

WEN FENG TSENG*, M. J. MARCINKOWSKI, E. S. DWARAKADASA†
Engineering Materials Group, and Department of Mechanical Engineering, University of Maryland, College Park, Maryland, USA

An extensive transmission electron microscopy study has been made of the structure of high and low angle grain boundaries in both ordered and disordered FeCo alloys which were electrochemically thinned from the bulk material. The grain boundaries observed were determined to be of the primary coincidence type and were found to contain numerous secondary grain-boundary dislocations. These secondary dislocations were either of the true grain-boundary types or else crystal lattice dislocations. The secondary grain-boundary dislocations were presumed to arise from the migration of the grain boundaries during grain growth and were frequently found to dissociate into crystal lattice dislocations arranged in the form of low angle boundaries within one of the adjacent grains.

1. Introduction

One of the most direct techniques for examining grain boundaries on a microscopic level is that of transmission electron microscopy (TEM). Perhaps the earliest TEM study showing that high angle grain boundaries contained dislocations as an integral part of their structure was that of Keh [1]. Since then, numerous TEM observations have shown similar results [2-6]. However, it has not been until rather recently that the grain-boundary substructure has begun to be elucidated by TEM techniques. Particularly significant in this respect are the studies of Gleiter and co-workers [7-10] along with those of Balluffi and associates [11-14]. Although the studies of Balluffi were carried out with grain boundaries of well defined orientations, they were prepared by evaporation techniques and were thus in the form of films. It was desired in the present study to examine grain boundaries of random orientation that were characteristic of those in bulk materials. Gleiter did, in fact, employ bulk samples in his studies; however, during the time of these investigations, the theory of grain-boundary dislocations was still in a rather embryonic state. It was with the aim of utilizing the theories of grain boundaries developed by the present authors in Part 1, which are also closely related to the theories of Bollmann [15], that the following TEM studies were carried out. In addition, it was decided to choose an alloy which could be obtained in both the ordered as well as the disordered state so as to assess the effects of atomic ordering on the grain-boundary substructure.

2. Experimental procedure

The alloy chosen for the present study contained nearly equiatomic proportions of Fe and Co. In particular, the Co concentration was 49.3 wt %. The choice of this specific alloy was dictated by the fact that through suitable heat-treatment, it could be prepared in either the fully ordered (CsCl type) or fully disordered (bcc) states. All of the details associated with alloy and sample preparation have previously been described in greater detail elsewhere [16, 17]. In summary, the samples were prepared in the form of rolled strips about 0.004 in. thick. These strips were in

*Now with The Department of Mechanical Engineering, University of Delaware, Newark, Delaware, USA.
†On leave from The Materials Research Group, Department of Metallurgy, Indian Institute of Science, Bangalore – 560012, India.

turn recrystallized by annealing for 15 min at 1050°C (γ phase region), rapidly cooling to room temperature and then annealing for 20 min at 850°C (α or bcc phase region). This particular heat-treatment resulted in a rather uniform grain diameter of about 0.0634 mm. The ordering and disordering heat-treatments were performed on the 0.0004 in. thick strips subsequent to the above heat-treatments. All samples were examined in the as-annealed condition. Specimens cut from the 0.004 in. thick strips were electrochemically thinned using a chrome-acetic acid electrolyte and examined in an Hitachi HU-200E electron microscope operating at 200 kV.

3. Grain-boundary dislocations

Before proceeding to the experimental results, it will be helpful to discuss in a reasonably concise manner the numerous types of grain-boundary dislocations (GBD) to be expected in an arbitrary grain boundary. For simplicity, the discussion will be restricted to simple cubic crystals [18, 19] where the rotation vector $\boldsymbol{\Omega}$ characterizing the grain boundary is along a cube direction. Furthermore, the magnitude of the rotation angle will be taken as 53.1°, i.e. a primary coincidence site angle. The coincidence site lattice (CSL) unit cell associated with this grain boundary is shown in Fig. 1 where the A's indicate atom positions within one of the two adjacent grains. The edge lengths associated with the CSL unit cell are given by a_{0c}, b_{0c} and c_{0c} where in the specific case illustrated in Fig. 1, $a_{0c} = b_{0c} \neq c_{0c}$.

The CSL unit cell can be further subdivided into smaller unit cells which are shown dashed in Fig. 1. These nave unit cell edge lengths given by a_{0DSC}, b_{0DSC} and c_{0DSC} where for the case shown in Fig. 1, $a_{0DSC} = b_{0DSC} \neq c_{0DSC} = c_{0c} = a_0$. The subscript DSC was first coined by Bollmann [15] to denote the lattice shown dashed in Fig. 1. The quantity a_0 is simply the unit cell edge length associated with the simple cubic crystal, or equivalently the distance of closest approach between the A atoms in Fig. 1.

The role of the CSL can be more simply seen by reference to the 53.1° symmetric tilt boundary shown in Fig. 2a where two neighbouring CSL

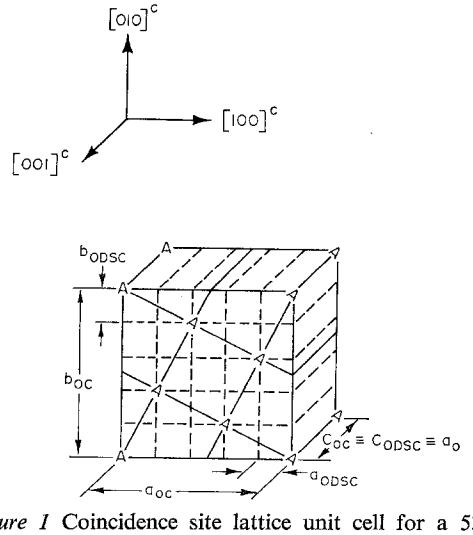

Figure 1 Coincidence site lattice unit cell for a 53.1° grain boundary in a simple cubic lattice.

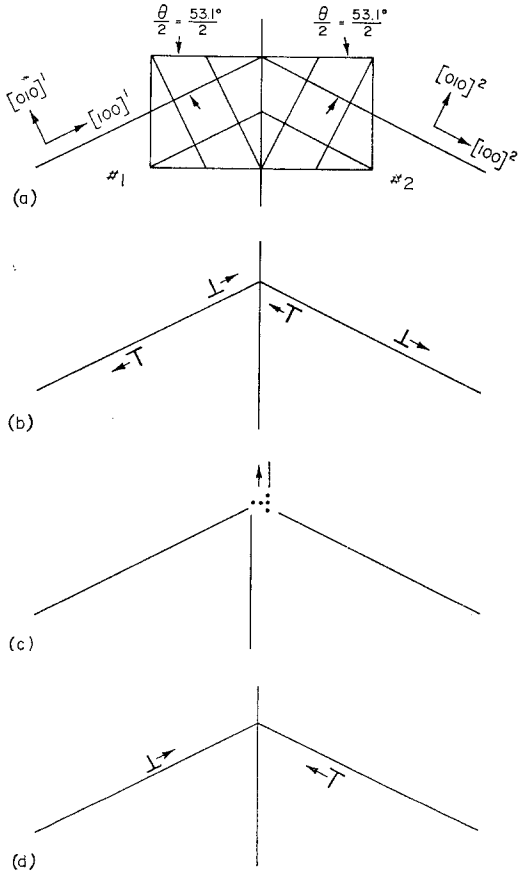

Figure 2 Primary slip planes associated with a 53.1° grain boundary in a simple cubic lattice; (a) before glide, (b) after nucleation of a pair of crystal lattice dislocations in adjacent grains, (c) after combination of the pair of crystal lattice dislocations to form a grain-boundary dislocation, (d) after dissociation of the grain-boundary dislocation into its two constiuent crystal lattice dislocations.

unit cells are drawn; one in grain no. 2, similar to that shown in Fig. 1, and the other in grain no. 1. Primary slip planes whose normals are $[010]^1$ and $[010]^2$ are indicated in the two adjacent grains by line extensions out of the CSLs. Fig. 2b shows the effect of nucleating a dislocation loop, i.e. a plus-minus dislocation pair in grains no. 1 and 2. The two inner dislocations can be visualized as moving towards the grain boundary to create the GBD shown dotted in Fig. 2c, while the outer two dislocations glide out of the crystal. The GBD shown in Fig. 2c may also be visualized as being associated with a grain-boundary ledge which can in turn decompose into two CLDs as illustrated in Fig. 2d. For the details of these particular processes, the reader is referred to earlier papers by the present authors [20-26].

Fig. 3 shows additional types of GBDs of both the edge and screw varieties. Except for quantitative differences such as sign and choice of slip plane, the GBDs shown in Fig. 3 are believed to represent qualitatively all of the basic horizontal types that can exist within a symmetric tilt boundary. The second and third columns show their corresponding dissociation into CLDs by glide and by climb, respectively. Note also that when a CLD lies in the grain boundary, as depicted in Fig. 3c′, d′ and i′, it is depicted as a GBD. The screw type GBDs obviously do not dissociate by climb so that the third column associated with these particular types is left vacant in Fig. 3. It is also seen that the GBDs are all derived from CLDs which lie on either the primary or the secondary slip systems but not combinations of the two since these are associated with a higher energy class of GBDs which will not be considered here [25, 19]. Fig. 3g′ and g″ also show the case where a pair of CLDs have been generated at the grain boundary without the necessity of GBDs.

It is a rather simple matter to obtain the Burgers vector of the GBDs shown in Fig. 3. Specifically, in those cases where the GBD is derived from CLDs in both grains such as in Fig. 3a′, b′, c′, f′, g′ and h′, the Burgers vector of the GBD can be expressed as follows [18, 25]:

$$\boldsymbol{b}_{GB} = \boldsymbol{b}_{CL}{}^{1} \pm \boldsymbol{b}_{CL}{}^{2}. \qquad (1a)$$

In the case of Figs. 3c′, d′ and h′, on the other hand,

$$\boldsymbol{b}_{GB} = \boldsymbol{b}_{CL}{}^{1}. \qquad (1b)$$

The magnitudes of $\boldsymbol{b}_{GB}$ are readily found from

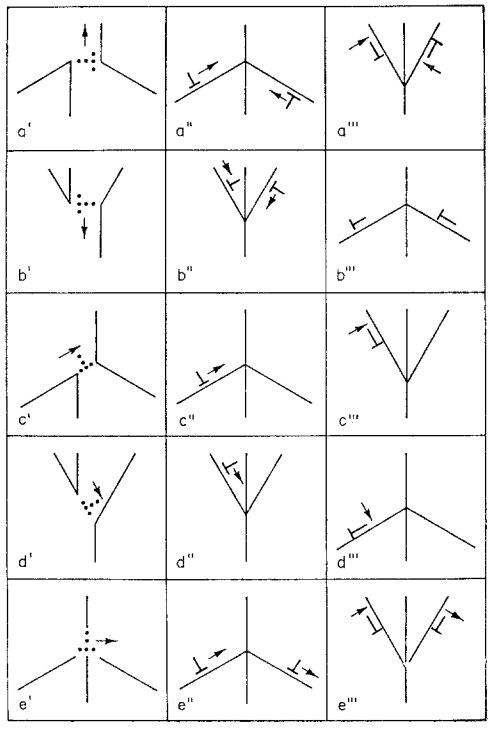

Figure 3 Various horizontal edge type grain-boundary dislocations (first column) which have decomposed by glide (second column) at a symmetric tilt boundary.

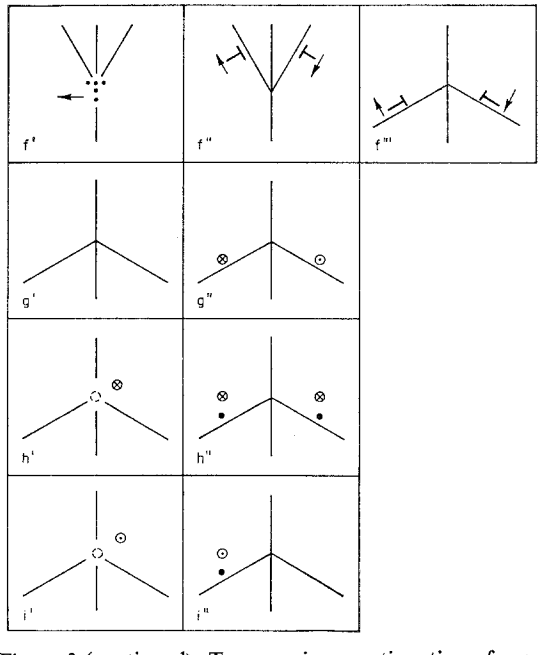

Figure 3 (continued). Top row is a continuation of preceding figures, while remaining figures represent various horizontal screw type grain boundary dislocations (first column) which have decomposed by glide (second column) at a symmetric tilt boundary.

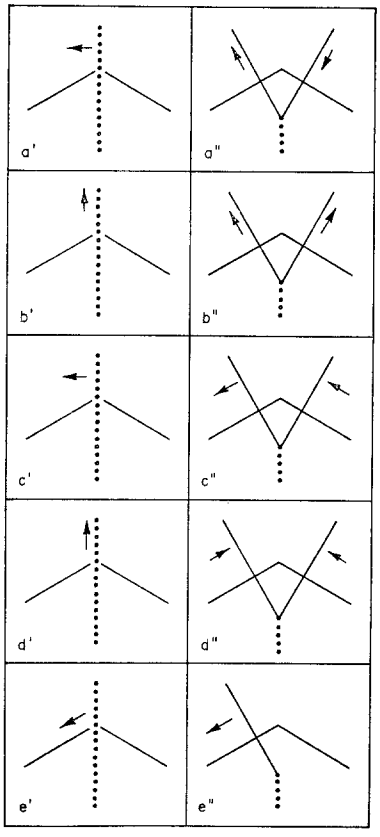

Figure 4 Various vertical edge and screw type grain-boundary dislocations (first column) which have decomposed by glide (second column) at a symmetric tilt boundary.

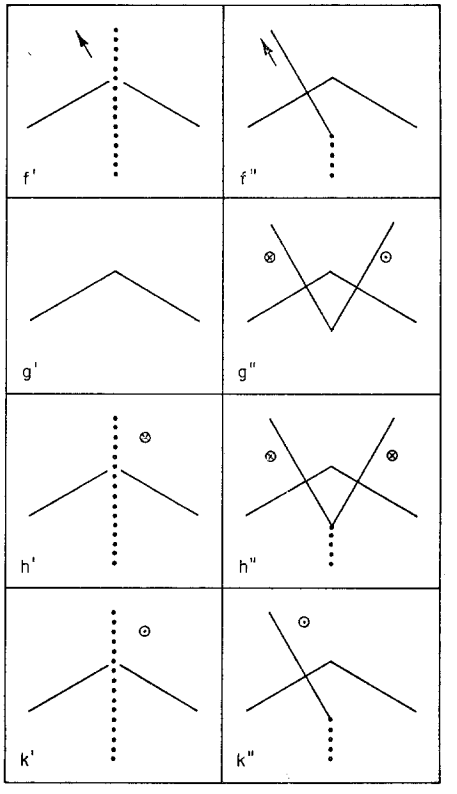

Figure 4 (continued). Top row is a continuation of the preceding figures, while remaining figures represent various vertical edge type grain-boundary dislocations (first column) which have decomposed by climb (second column) at a symmetric tilt boundary.

the geometries of Figs. 2 and 3. For example, in the case of Fig. 3a′, or equivalently, Fig. 2

$$| \boldsymbol{b}_{\mathrm{GB}} | = 2a_0 \sin \left[\frac{\theta}{2}\right] \cdot \qquad (2)$$

Reference to Fig. 1 shows that $\boldsymbol{b}_{\mathrm{GB}}$ for the case shown in Fig. 3a′ can be expressed either in terms of the CSL or else in terms of the DSC lattice. In particular in terms of the CSL

$$\boldsymbol{b}_{\mathrm{GB}}{}^{\mathrm{CSL}} = \frac{2N}{(N^2 + M^2)} b_{0\mathrm{c}} [010]^{\mathrm{c}} \qquad (3a)$$

while in terms of the DSC

$$\boldsymbol{b}_{\mathrm{GB}}{}^{\mathrm{DSC}} = 2 b_{0\mathrm{DSC}} [010]^{\mathrm{c}} \qquad (3b)$$

where N and M are simply integers which correspond to the number and interplanar separation of the CLDs which comprise a coincidence angle grain boundary given by [18, 25]

$$\tan \left(\frac{\theta_{\mathrm{c}}}{2}\right) = \frac{N}{M} \cdot \qquad (4)$$

For the specific case shown in Fig. 1 where $\theta_{\mathrm{c}} = 53.1°$, $N = 1$ and $M = 2$. It is also important to note that the GBDs illustrated in Fig. 3 are all referred to an already existing coincidence angle grain boundary given by Equation 4. In this respect they may be referred to as secondary GBDs, as was first done by Bollmann [15]. However, the primary coincidence angle boundary itself is comprised of GBD which may be termed primary GBDs. It turns out that for primary GBDs, $N = 1$ in Equation 4, while for secondary GBDs, $N = 2$ in this Equation [18]. Higher values of N may be defined [26]; however, this will not be considered in the present analysis. Secondary GBDs may also be thought of as those GBDs which enable a primary coincidence

grain boundary to alter its nature either by transforming it into another primary coincidence grain boundary or by changing its symmetry [18, 19, 25]. Not shown in Fig. 3 is the break-up of a single GBD into a pair of GBDs lying within the boundary; however, these can be readily derived from the figures.

Another class of GBDs within a symmetric tilt boundary may be referred to as those of vertical type such as shown in the first column of Fig. 4. The second column of this figure shows the corresponding decomposition of these GBDs into their constituent CLDs, either by glide (4a″ to f″) or by climb (4g″ to k″). Finally, the first column of Fig. 5 illustrates the various kinds of GBDs of either edge or screw type which can exist within a symmetric twist boundary. The second column shows the decomposition of these GBDs into their corresponding CLDs. The solid lines in this second column indicate that the CLDs lie toward the right of the boundary, while the dashed lines signify that the CLDs lie to the left of the boundary. The detailed behaviour of GBDs which comprise twist boundaries has been treated in detail in [26]. All of the GBDs illustrated in Figs. 3, 4 and 5 can be generated by grain-boundary migration and need not involve plastic deformation occasioned by an externally applied stress. With respect to any given grain boundary, the GBDs illustrated in Figs. 3, 4 and 5 may not be in their lowest energy configuration, so that rearrangement may occur. This is most easily visualized by reference to Fig. 6a which shows a square grain bounded by primary GBDs of the type shown in Fig.

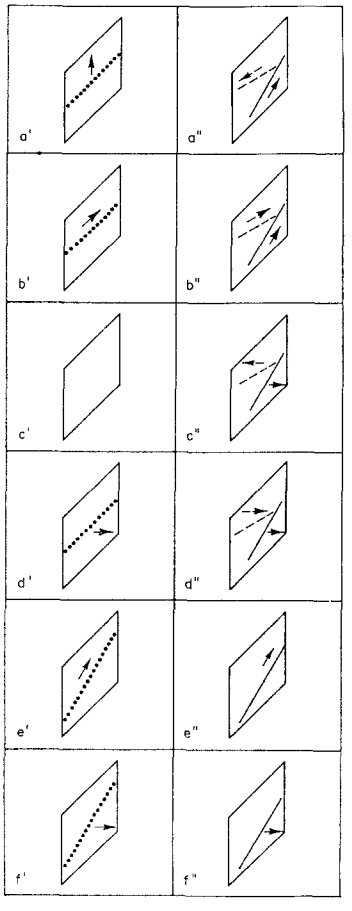

Figure 5 Various edge and screw type grain-boundary dislocations (first column) which have decomposed by either glide or by climb (second column) at a symmetric twist boundary.

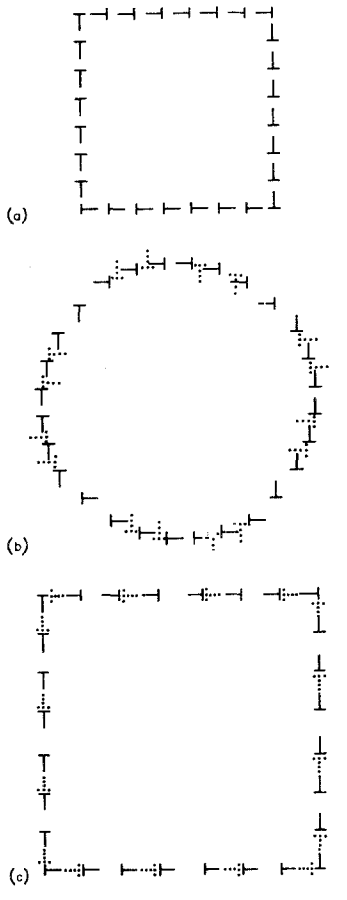

Figure 6 Growth of the grain boundary shown in Fig. 6a by the introduction of secondary grain-boundary dislocations to give the configurations shown in (b) and (c).

3e′. It is now possible for the square grain in Fig. 6a to expand into the circular grain illustrated in Fig. 6b by grain-boundary migration. Such grain-boundary migration is equivalent to the introduction of secondary GBDs such as is shown in Fig. 3a′ [19, 24]. These secondary grain-boundary dislocations in Fig. 6b are drawn dotted to distinguish them from the primary GBDs which are indicated as solid lines. Inspection of Fig. 6b shows that many of the secondary GBDs have parallel Burgers vectors and lie on very nearly the same plane. Long range stress fields, and thus high energies, arise from such arrays [27, 28]. It is, however, possible to lower the energy of the circular grain-boundary configuration in Fig. 6b by allowing the secondary GBDs to rearrange themselves into the configuration shown in Fig. 6c. Such rearrangement requires both glide and climb of these secondary GBDs. Since all of the secondary and primary GBDs in Fig. 6c are vertically aligned, it follows that the stress fields associated with ths grain boundary are of short range character so that the boundary is of low energy. Also important to note is that during the rearrangement from Fig. 6b and c the secondary GBDs have been transformed from the type shown in Fig. 3a′ to that shown in Fig. 3f′. It also follows that if the grain boundary shown in Fig. 6a had a misorientation angle θ originally associated with it, then the misorientation angle associated with the grain boundary shown in Fig. 6c is given by $\theta - \Delta\theta$ where $-\Delta\theta$ is the decrease in grain-boundary misorientation occasioned by the introduction of secondary GBDs. The angle is of course decreased since the secondary GBDs are of opposite sign to those of the primary GBDs.

If the grain illustrated in Fig. 6a is allowed to shrink, on the other hand, by grain-boundary migration, the grain-boundary configuration shown in Fig. 7a obtains. Using arguments similar to those employed in Fig. 6, the energy of the grain boundary in Fig. 7b can be decreased by allowing the GBD rearrangement which gives rise to Fig. 7b to take place. Here again, both the primary and secondary GBDs are vertically aligned, and since both are of the same sign, the misorientation angle associated with this boundary is given by $\theta + \Delta\theta$, where $\Delta\theta$ is the contribution owing to the secondary GBDs. With the above considerations in mind, we are now in a position to discuss the following experimental observations.

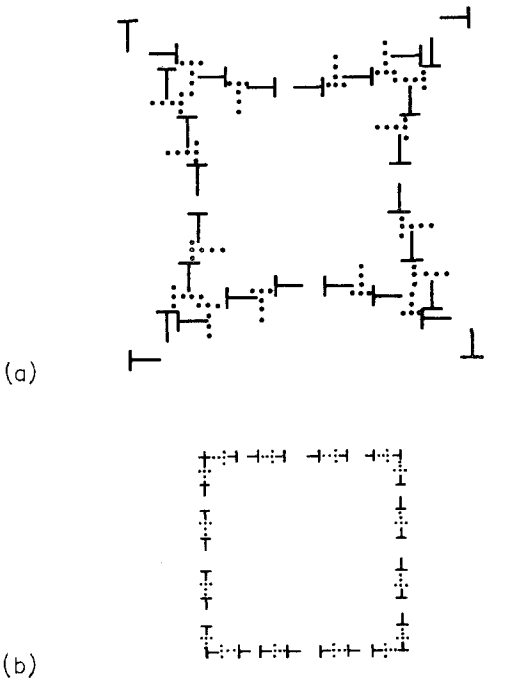

Figure 7 Shrinkage of the grain boundary shown in Fig. 6a by the introduction of secondary grain-boundary dislocations to give the configurations shown in (b) and (c).

4. Experimental results and discussion

Fig. 8a shows a transmission electron micrograph composite of a grain boundary observed in a disordered undeformed FeCo foil. The grain boundary is seem to contain a very high density of GBDs. Furthermore, the grain boundary is seen to be pinned by the circular inclusion located at the right centre of the figure. Before any analysis can be made of this boundary, it is first necessary to determine both the direction as well as the magnitude of the rotation axis Ω associated with the grain boundary. This is done by first referring to both Figs. 1 and 2a which show that any grain boundary has associated with it three crystallographic planes which are common to the two adjacent crystals. These are parallel to $[100]^c$, $[010]^c$ and $[001]^c$. These three common planes can be determined in the case of Fig. 8a by using the selected area diffraction patterns (SADP) shown therein to prepare the corresponding stereographic projections shown in Fig. 8b. The superscript 1 refers to the grain on the left of the boundary in Fig. 8a, while the superscript 2 designates the grain to-

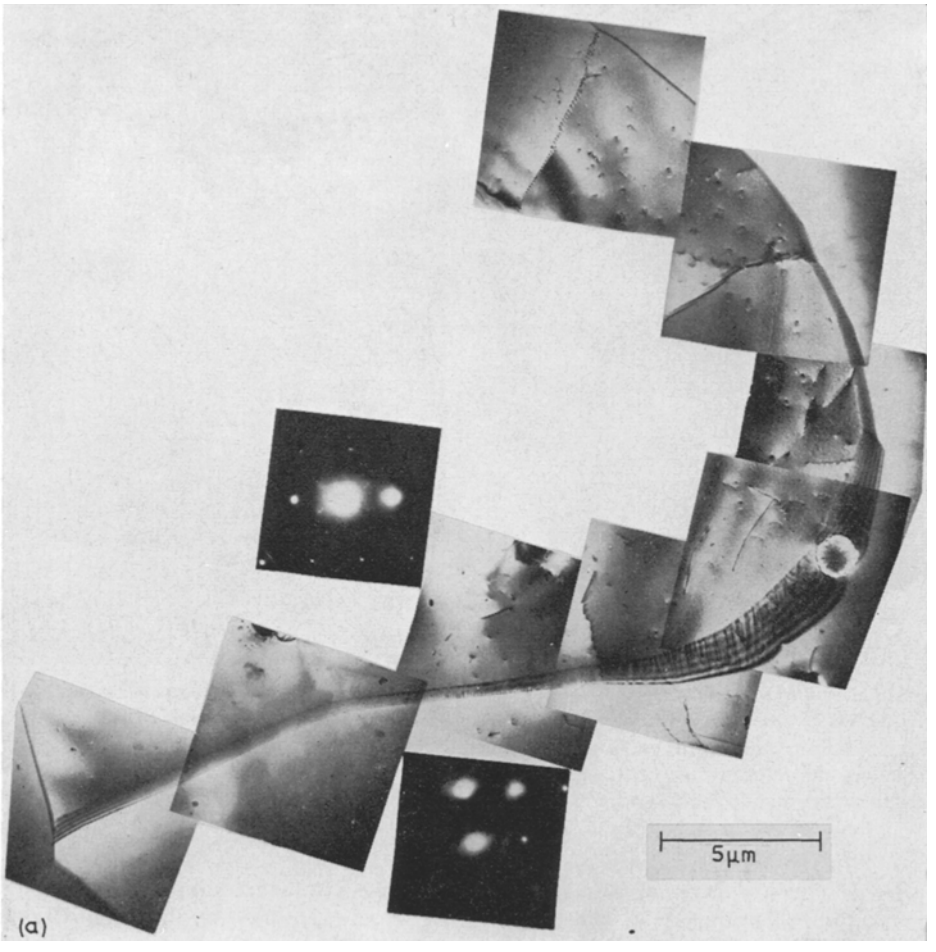

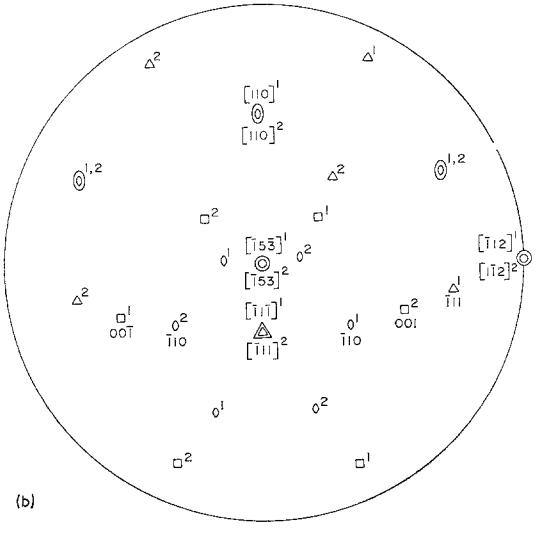

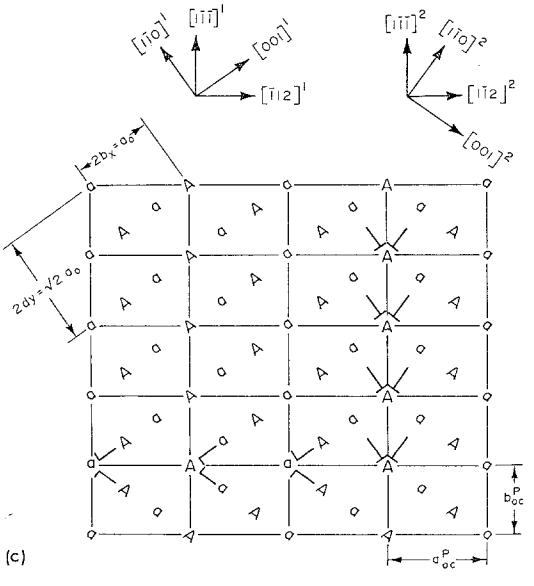

Figure 8 a b and c.

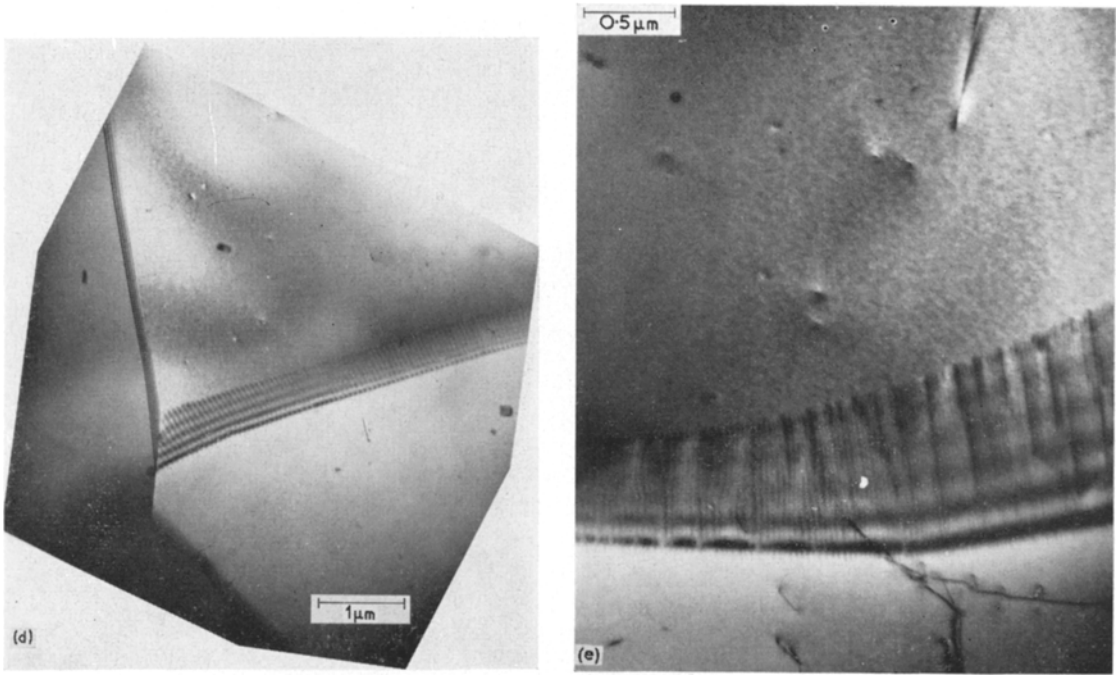

Figure 8 (a) Bright field transmission electron micrograph composite showing secondary grain-boundary dislocations in a disordered FeCo alloy. (b) Stereographic projections of the two grains associated with the grain boundary shown in (a). (c) Schematic illustration of the primary grain-boundary dislocation configuration associated with the grain boundary shown in (a). (d) Enlargement of lower left hand portion of the grain boundary shown in (a). (e) Enlargement of the middle right hand portion of the grain boundary shown in (a).

wards the right. There is an ambiguity in plotting stereographic projections from the SADPs shown in Fig. 8a. In particular, the SADPs give only those poles which lie on the periphery of the circle shown in Fig. 8b. This makes each SADP ambiguous with respect to a rotation of π about its normal, resulting in four possible orientation relationships between the two grains shown in Fig. 8a. Fortunately, however, only one of these combinations is consistent with the predictions of Part 1; namely, the one shown in Fig. 8b. In accordance with Figs. 5 and 6 of Part 1, $\boldsymbol{\Omega}$ is seen to lie along $[1\,1\,0]^1$ or $[1\,1\,0]^2$ with a magnitude of 70.5° so that it corresponds to a primary coincidence angle.

Referring to the results obtained in Part 1, it was next decided to construct the primary GBD structure associated with the grain boundary shown in Fig. 8a. This is illustrated in Fig. 8c where, for convenience, the $[1\,1\,0]^1$ or $[1\,1\,0]^2$ rotation axes were chosen normal to the drawing rather than the actual foil normals of $[\bar{1}\,5\,\bar{3}]^1$ or $[\bar{1}\,5\,3]^2$. This amounts to a 60° rotation of the foil normal about the $[1\,\bar{1}\,2]^2$ or $[\bar{1}\,1\,2]^1$ axis. It is immediately apparent from this figure that the grain boundary is comprised of full and half GBDs of the primary type. Furthermore, their spacings are given by $a_{0c}{}^{P}$ and $b_{0c}{}^{P}$ which corresponds to $a_0/\sqrt{3}$ and $\sqrt{2}\,a_0/\sqrt{3}$, respectively, i.e. between 1.65 and 2.35 Å, respectively. These distances are below the resolution of the present microscope and obviously much below the spacing between the GBDs shown in Fig. 8a, which range from about 600 Å in the lower left hand corner of the figure to about 300 Å near the inclusion toward the right centre of the figure. Higher magnification transmission electron micrographs of these areas are shown in Fig. 8d and e, respectively. Clearly then the GBDs observed in Fig. 8a must be of the secondary type. It is next of importance to determine the nature of these secondary GBDs. Since the line direction of the GBDs is approximately parallel to the rotation axis $\boldsymbol{\Omega}$ associated with the grain boundary, they must correspond to one of the types shown in Fig. 3. From the discussions relating to Fig. 6c and 7b, it follows that the GBDs are of the secondary type illustrated in

Fig. 3f'. Furthermore, nearly all of the secondary GBDs observed in Fig. 8a lie within the nearly horizontal portion of the grain boundary shown in Fig. 8a, i.e. that portion of the grain boundary situated below the inclusion. From Part 1 and Fig. 8c, the Burgers vectors of these secondary GBDs have magnitudes given by $2a_0/\sqrt{3}$ while from Fig. 8b, their direction is along $[\bar{1}\,1\,\bar{1}]^1$ or $[\bar{1}\,1\,1]^2$. It is apparent that since the present samples were undeformed, the secondray GBDs arise as a result of the migration and subsequent pinning of the grain boundary by the circular inclusion lying toward the right centre of Fig. 8a. It is also possible to calculate $\Delta\theta$ from the relationship given by $\Delta\theta = b_{GB}/h$, where from the above discussion, $b_{GB} = 2a_0/\sqrt{3}$, and h ranges from 300 to 600 Å giving $\Delta\theta \simeq 0.5$ to 0.3°.

All of the GBDs discussed with respect to Fig. 8a were of the edge type and thus consisted of parallel arrays. Fig. 9a, on the other hand, shows a grain boundary in a fully ordered FeCo alloy which is seen to consist of a nearly orthogonal cross-grid of GBDs. In order to determine the nature of this grain boundary, stereographic projections were prepared from the SADPs given in Fig. 9a and these are shown plotted in Fig. 9b. Again, as in the case of Fig. 8c, the superscript 1 refers to the grain towards the left of the boundary, while the superscript 2 refers to the grain towards the right of the boundary. In addition, the orientations shown in Fig. 9b represent the closest fit between all of the various combinations attainable from the SADP of Fig. 9a which are consistent with the predictions of Part 1. Specifically, in accordance with Fig. 8 of Part 1, $\boldsymbol{\Omega}$ is seen to lie along $[\bar{1}\,\bar{1}\,2]^1$ or $[\bar{1}\,\bar{1}\,2]^2$ and has a magnitude of 68°. This is in reasonably close agreement with a primary coincidence angle of 62.8° predicted in Part 1, considering the uncertainties associated with the analysis of SADPs [29]. It is next a relatively simple matter to determine the primary GBD configuration which constitutes the primary coincidence grain boundary associated with Fig. 9a in a manner similar to that done in Fig. 8d. Again, however, the closest spacing between the grain-boundary dislocations in Fig. 9a shows them to be about 400 Å apart; a distance much too large for primary GBDs, so that they must be of secondary type.

Fig. 10 gives a schematic illustration of the manner in which the transmission electron micrograph of Fig. 9a may be visualized. In

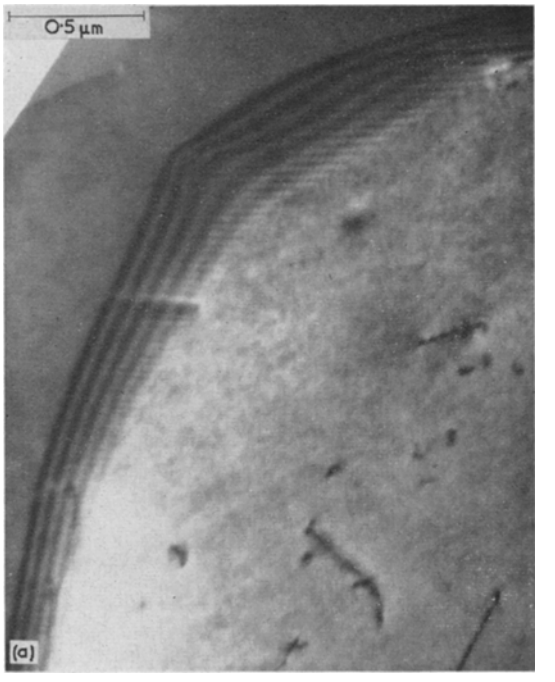

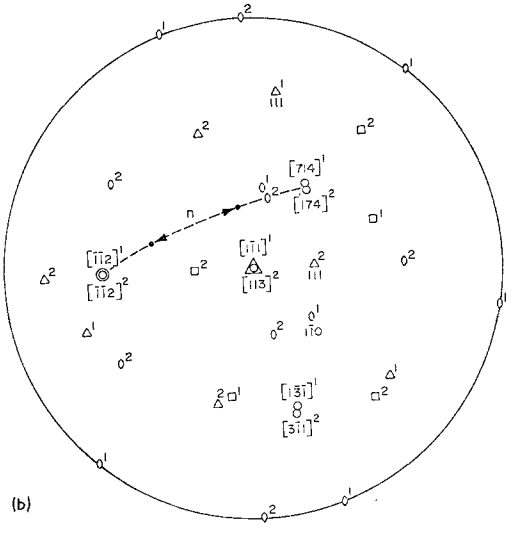

Figure 9 (a) Bright field transmission electron micrograph showing secondary grain-boundary dislocations in a fully ordered FeCo alloy. (b) Stereographic projections of the two grains associated with the grain boundary shown in (a).

particular, an orthogonal three-dimensional GBD array is constructed in the manner described in connection with Fig. 13a of Part 1. One of the faces is then made oblique, i.e. the top face MNOP in Fig. 10. The resulting primary GBDs are shown in solid outline while the

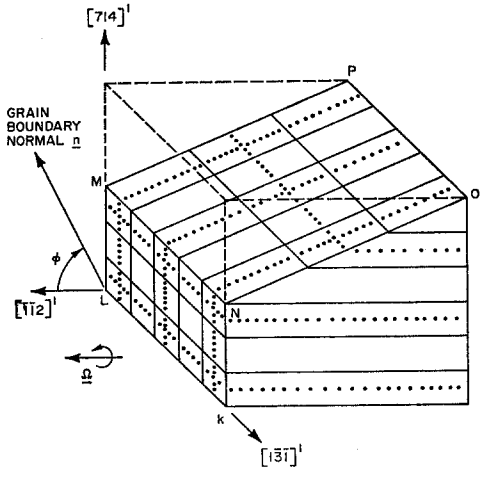

Figure 10 Schematic illustration of grain boundary corner shown in Fig. 9a.

secondary GBDs are illustrated by dotted lines. To a simple approximation, the GBD configuration shown in face MNOP of Fig. 10 can be visualized as corresponding to the GBD array contained in the boundary toward the right of the bend in Fig. 9a. On the other hand, the GBD configuration shown in face KLMN of Fig. 10 corresponds approximately to the orthogonal GBD array observed in the boundary toward the left of the bend in Fig. 9a. Strictly speaking, the normal to the grain boundary **n** in Fig. 9a varies along a great circle within the range of angles lying between the two arrows shown in Fig. 9b. The pole associated with this great circle is either $[1\,\bar{3}\,\bar{1}]^1$ or $[3\,\bar{1}\,1]^2$. However, this refinement does not alter the qualitative picture of the GBD array given by Fig. 10; namely that the GBD configuration contained within the surface KLMNOP corresponds to the experimentally observed configuration shown in Fig. 9a. It follows from the analysis of Part 1 and Fig. 10 that the orthogonal network of secondary GBDs in Fig. 9a corresponds to two sets of screw dislocations with Burgers vectors which lie along $[7\,1\,4]^1$ and $[1\,\bar{3}\,\bar{1}]^1$. Since these screw type GBDs lie at right angles to one another, there is no tendency for them to react because no reduction of energy is occasioned by such a reaction. Another conclusion that can be drawn from the orthogonality of the GBDs toward the left of Fig. 10 is that they are similar to the type shown in Fig. 5b′, but with the CLDs from the two adjacent grains lying on secondary slip planes [26]. The GBD in Fig. 5b′ is of the primary type. If these GBDs were of the type shown in Fig. 5e′, i.e. CLDs which were within the grain boundary, they would not lie at right angles to one another and would, therefore, react to form a hexagonal GBD network [30, 31]. As will be seen later, this observation provides a powerful method for distinguishing between true GBDs of the type shown in Fig. 5b′ and GBDs which are in fact CLDs lying within the grain boundary as shown in Fig. 5e′. As will also be later demonstrated, although atomic ordering has a pronounced effect on CLDs lying in the grain boundary, it has no effect on the morphology of true GBDs.

It was next decided to carry out a dark field analysis of the secondary GBD structure. This can be seen in Fig. 11a which is a dark field transmission electron micrograph of a grain boundary in a fully ordered FeCo alloy using the strong $1\,1\,\bar{2}$ reflection associated with grain no. 2. This same area is shown in Fig. 11b but the strong $1\,1\,0$ reflection associated with grain no. 1 now allowed to form the dark field image. In both cases, in order to increase the GBD resolution, the dark field image was formed by aligning the given diffracted beam along the electron microscope column [29]. The best choice of stereographic projections associated with the pair of SADPs in Figs. 11a and b is shown in Fig. 11c. It follows from this figure that the rotation axis associated with the grain boundary in Fig. 11a and b is along $[1\,1\,\bar{2}]^1$ or equivalently $[1\,1\,\bar{2}]^2$ and is of magnitude 61.4°, a value in good agreement with the primary coincidence angle of 62.8° determined in Part 1.

A highly schematic illustration of the grain boundary of Fig. 11a is shown in Fig. 12. In particular, the view normal to the drawing can be visualized as being obtained by first rotating a vertical twist boundary which has one of its coincidence site lattice unit cell edges (either a_{0c} or b_{0c} in Fig. 1) initially in the plane of the drawing, by approximately 30° about the $[0\,0\,1]^c$ or $[1\,1\,\bar{2}]^1$ axis. The grain boundary is then rotated about an axis normal to $[0\,0\,1]^c$. The resulting primary GBD configuration is then very much the same as that predicted by Fig. 13d in Part 1 and is shown in Fig. 12a. Introduction of the secondary GBDs gives rise to the configuration shown in Fig. 12b. Again, as in the previous two transmission electron micrographs, it is only the secondary GBDs which are visible in Fig. 11a and b. Perhaps the most interesting aspect of Fig. 11a and b is the break-up of

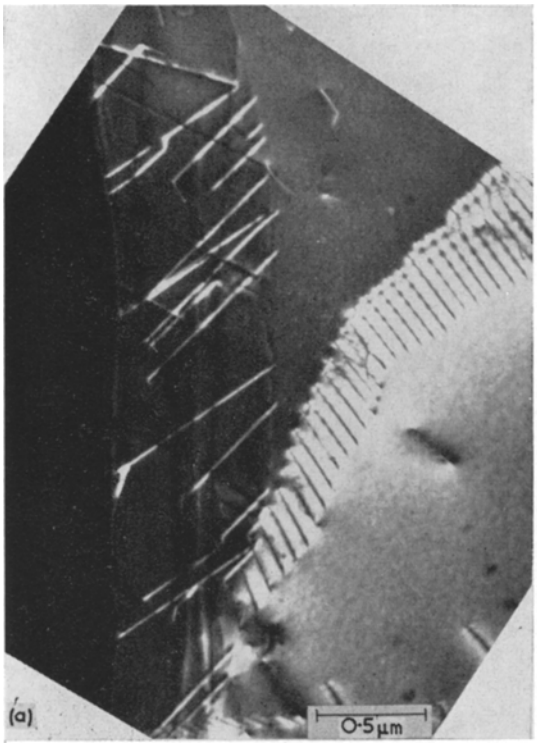

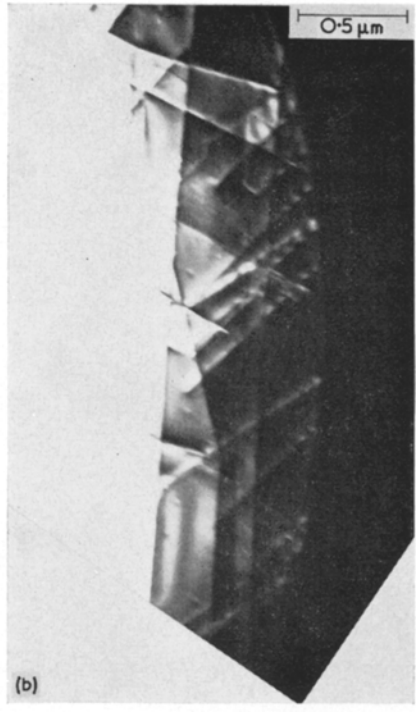

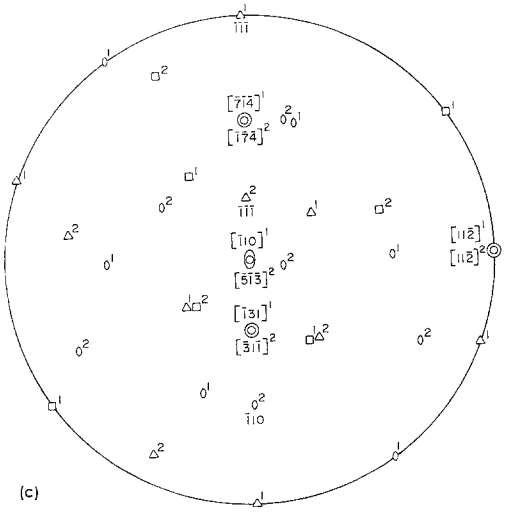

Figure 11 (a) Dark field transmission electron micrograph obtained with the $11\bar{2}$ reflection associated with the grain on the right, showing secondary grain-boundary dislocations in a fully ordered alloy. (b) Dark field transmission electron micrograph obtained with the 110 reflection associated with the grain on the left, from the same area shown in (a). (c) Stereographic projection of the two grains associated with the grain boundary shown in Fig. (a) and (b).

the GBDs. The schematic interpretation of some of these GBD dissociations is shown by the solid line segments in Fig. 12c. It follows from Fig. 5b′ that the GBDs can be visualized as breaking up into their corresponding CLDs, one of which is associated with each grain. That this is indeed the case can be seen in Fig. 11a, where one of the CLDs associated with each dissociated GBD appears white and is in strong contrast, indicating that it is associated with grain no. 2 from which the dark field image is being formed. On the other hand, the second CLD associated with each dissociated GBD appears dark and is only faintly visible, indicating that it resides within grain no. 1 which is not contributing to the image. However, when the dark field image is formed by using the strongest reflection from grain no. 1, the CLD segments of the GBDs which lie within grain no. 1 appear white and show strong contrast, whereas those CLD segments in grain no. 2 are nearly invisible. In most cases only one of the two CLD arms of a dissociating GBD can be observed in Fig. 11a, as is also indicated schematically near the top of Fig. 12c, and this is owing to the fact that one of the arms is nearly normal to the foil. Also of significance in Fig. 11a is that many of the CLDs arising from the dissociating GBD are

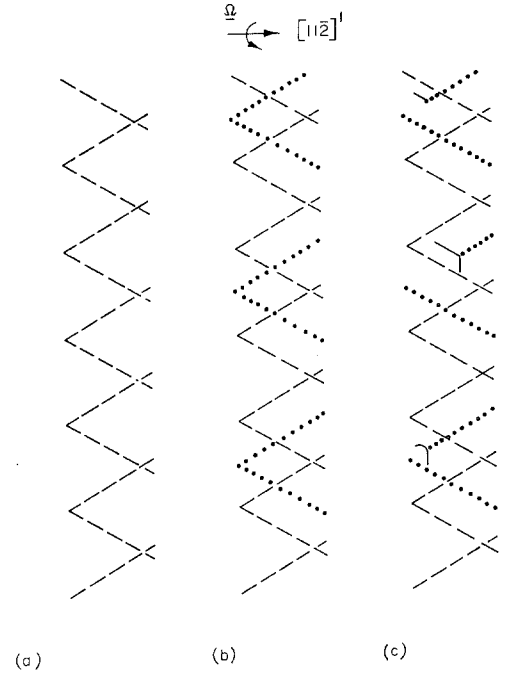

Figure 12 Schematic interpretation of the grain boundary shown in Fig. 11a and b. (a) only the primary grain-boundary dislocations are present, (b) both primary and secondary grain-boundary dislocations are present, (c) after dissociation of some of the secondary grain-boundary dislocations.

being rejected from the grain boundary in the form of dislocation walls or low angle tilt boundaries.

Thus far, most of the GBDs observed have been of the type derived from Equation 1a, i.e. combinations of CLDs from the adjacent grains. Fig. 13a, on the other hand, shows a high angle grain boundary (upper portion of the figure) in a disordered FeCo alloy to which are attached a pair of low angle boundaries. That the upper grain boundary is indeed one of high angle is attested to be the strong fringe pattern contrast associated with this boundary [29]. Unfortunately, it was not possible to identify either the grain-boundary rotation vector or its magnitude since the SADPs associated with the two adjacent grains consisted of only one row of excited reflections. It is clear from Fig. 13a that the GBDs within the high angle boundary are of the type given by Equation 1b and illustrated in Figs. 3c′, d′, and 5e′, i.e. they are CLDs which lie in the boundary. This is readily apparent from the schematic illustration of Fig. 13a in Fig. 13b which clearly shows the break-up of a hexagonal

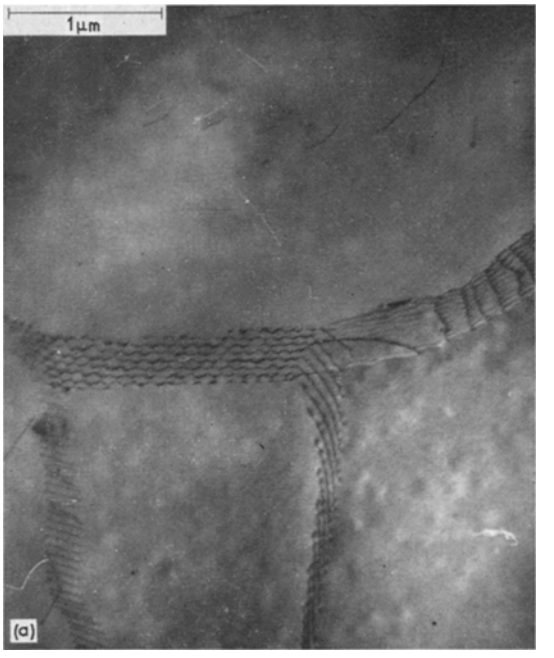

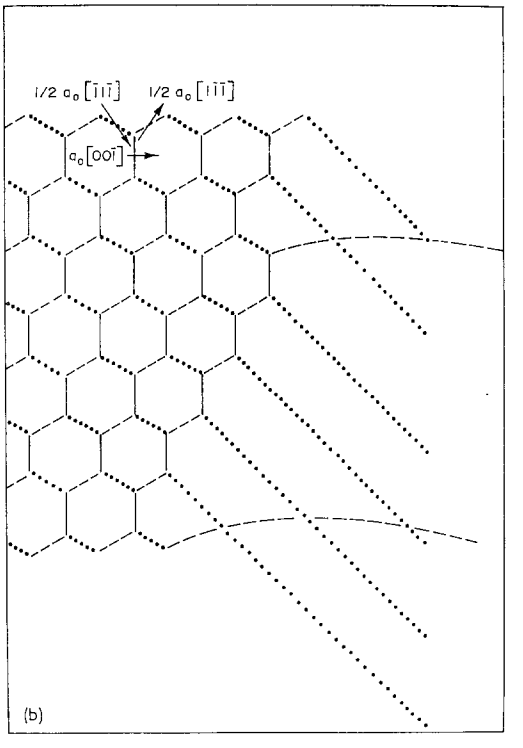

Figure 13 (a) Bright field transmission electron micrograph of crystal lattice dislocations within a high angle grain boundary of a disordered FeCo alloy. (b) Schematic illustration of the transmission electron micrograph shown in (a).

array of CLDs which lie within the grain boundary into two distinct parallel CLD arrays, one of which stays within the boundary (dashed lines) and lies towards the right of the hexagonal array and the other of which extends vertically downward into the bottom-most grain (dotted lines). It is apparent from Fig. 13b that three distinct types of Burgers vectors are involved in the network and these are so indicated. The dislocation segments within the hexagonal network that are drawn as solid lines are simply the result of the reaction between the original cross grid of screw type dislocations with Burgers vectors $\frac{1}{2}\, a_0\, [\bar{1}\,1\,\bar{1}]$ and $\frac{1}{2}\, a_0\, [1\,\bar{1}\,\bar{1}]$. Again, it is to be emphasized that a cross-grid of screw type CLDs can react within a grain boundary to form a hexagonal network. On the other hand, a cross grid of GBDs such as those discussed in connection with Fig. 9a are at right angles to one another and will not react. This provides a powerful method of distinguishing between these two distinct types of dislocations within a high angle boundary.

All of the GBDs observed thus far were seen to move out of the grain boundary by processes which mostly involved climb. Fig. 14a, on the other hand, shows the generation of CLDs from GBDs near a triple point in a fully ordered FeCo alloy. The detailed analysis of the crystallography of the three distinct types of high angle grain boundaries in this figure are not necessary in the analysis to follow and will, therefore, not concern us here. It is of interest, however, to point out that the three grain boundaries associated with the triple point junction in Fig. 14a had rotation axes of [100], [110] and [110] of magnitude given by 37°, 83° and 20°, respectively, in good agreement with the theoretically predicted values of 36.9°, 70.5° and 20°, respectively, associated with primary coincidence site boundaries treated in Part 1. Since slip traces emanate from the GBDs in these figures, it follows that the GBDs have decomposed into CLDs by glide. In fact, the actual decomposition could indeed be observed within the electron microscope, and was most likely owing to thermal stresses induced by the electron beam. An approximate schematic illustration of the GBD decomposition processes taking place in Fig. 14a is shown in Fig. 14b. The dashed lines outline the grain-boundary traces while the dotted lines correspond to the slip traces, whereas, the solid lines correspond to the dislocations. It follows from this drawing that the

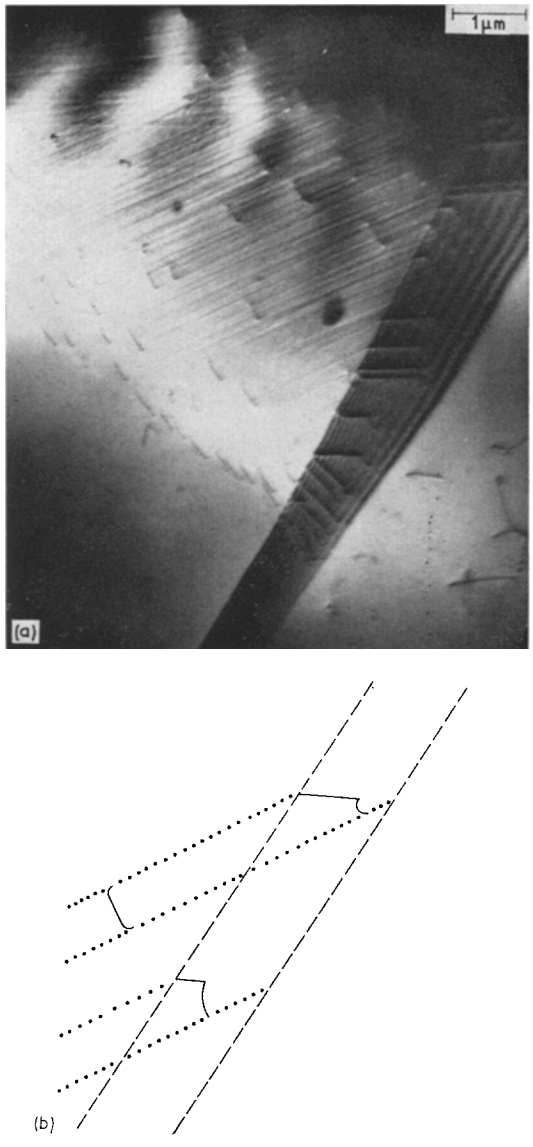

Figure 14 (a) Bright field transmission electron micrograph of grain-boundary dislocation decomposition near a triple point junction in a fully ordered FeCo alloy. (b) Schematic illustration of transmission electron micrograph shown in (a).

GBDs are of the CLD type shown in Figs. 3c′ or 5e′. Furthermore, some of the GBDs are of multiple strength since on occasion, more than one CLD is associated with a single slip trace as can be seen near the top of Fig. 14b.

Fig. 15a shows another interesting GBD configuration associated with a high angle grain boundary in a disordered FeCo alloy. In fact, many of the GBDs as well as the CLDs in the

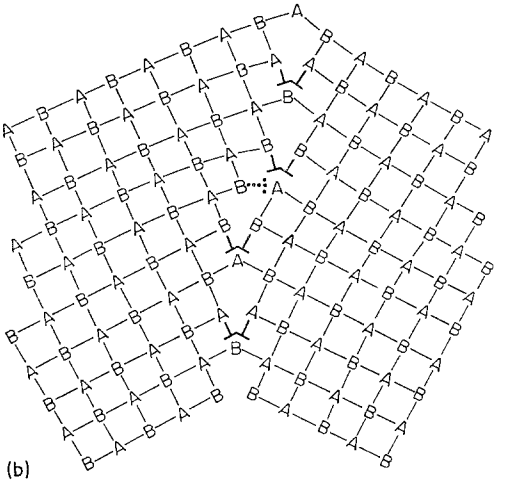

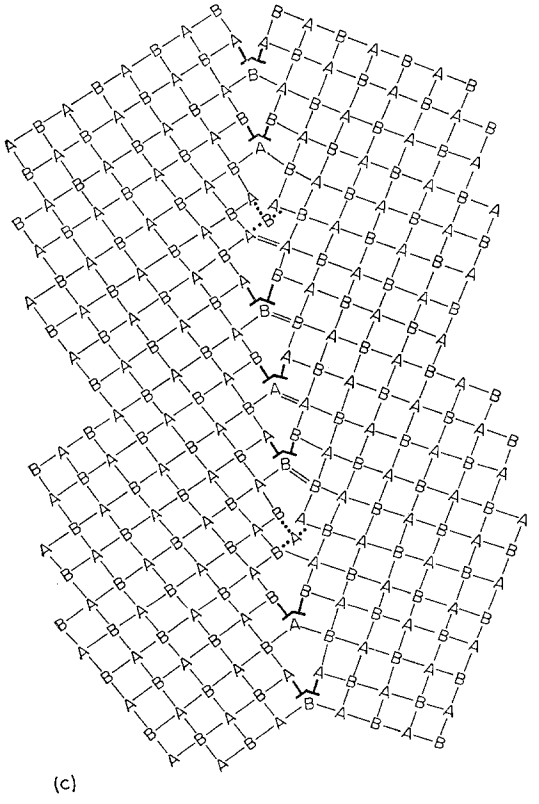

Figure 15 (a) Bright field transmission electron micrograph showing grain-boundary dislocation pairs in a quenched but incompletely disordered FeCo alloy. (b) Grain-boundary dislocation of the type shown in Fig. 3a′ in an ordered lattice where the grain-boundary rotation angle is 53.1°. (c) Coupled pair of grain-boundary dislocations of the type shown in Fig. 3c′ in an ordered lattice where the grain-boundary rotation angle is 53.1°.

grain towards the right are seen to be paired. This dislocation pairing is undoubtedly brought about by imperfect quenching which leads to the formation of a small but finite degree of long range order within the sample [32]. However, it is not obvious *a priori* what effect atomic ordering should have on the configuration of secondary GBDs. In order to understand this effect, reference is made to Fig. 15b which shows a secondary GBD (drawn dotted) of the type shown in Fig. 3a′, i.e. one composed of a pair of CLDs of opposite sign from the two adjacent grains. The dislocations outlined by heavy solid lines are the primary GBD and comprise the primary coincidence grain boundary for which the magnitude of $\boldsymbol{\Omega}$ is 53.1°. It is apparent from inspection of Fig. 15b that no atomic disorder is associated with a GBD of this type. Fig. 15c, on the other hand, shows a pair of GBDs of the type shown in Fig. 3c′, i.e. CLDs lying within the grain boundary. Unlike the case of Fig. 15b, there is a ribbon of incorrect nearest neighbour AA and BB atom bonds (shown by double lines) connecting the two GBDs. The dislocation pair

shown in Fig. 15c is thus a superlattice GBD similar to that described for a single crystal [32]. The equilibrium extension of the superlattice GBD is determined by the force equilibrium arising from the elastic repulsion between the pair of GBDs and the attraction owing to the wrong nearest neighbour atom pairs separating the GBDs. Thus, as mentioned earlier, another method is established for differentiating between true GBDs and CLDs which lie within the grain boundary. It is also apparent from the slip traces emanating from the lower left hand portion of the grain boundary in Fig. 15a that some of the GBDs are dissociating into CLDs.

All of the grain boundaries examined thus far correspond very nearly to primary coincidence boundaries, i.e. $N = 1$ in Equation 4. This is in accordance with the postulate that boundaries of this type have associated with them minimum energies [10]. The secondary GBDs contained within these primary grain boundaries are undoubtedly owing to the irregular migration of the grain boundaries by grain growth.

5. Summary and conclusions

A detailed transmission electron microscopy study has been carried out of the dislocation structure of grain boundaries in both ordered and disordered FeCo alloys which were electrochemically thinned from the bulk material. It was found that the grain boundaries were of the type characterized by primary coincidence site lattices which frequently contained secondary grain boundary dislocations. The secondary grain-boundary dislocations, on the other hand, were either true grain-boundary dislocations or else consisted of crystal lattice dislocations lying within the grain boundaries. The secondary grain-boundary dislocations are postulated to arise as a result of grain-boundary migration and frequently decompose into crystal lattice dislocations which are arranged in the form of low angle boundaries.

Acknowledgements

The authors would like to express their thanks to Dr K. Sadananda of The University of Maryland, Dr E. S. P. Das of The Argonne National Laboratory, Professor R. W. Balluffi of Cornell University, Professor J. P. Hirth of The Ohio State University and Dr W. H. Cullen, Jun. of the Naval Research Laboratory for a number of stimulating discussions concerning grain-boundary dislocations. They would also like to acknowledge the expert technical assistance of Mr M. E. Taylor, Jun. during the course of the present investigation. Financial support for the present study was provided by The National Science Foundation under Grant No. GH-32262.

References

1. A. S. KEH, "Direct Observation of Imperfections in Crystals" (edited by J. G. Newkirk and J. H. Wernick) (Interscience, New York, 1962) p. 213.
2. R. M. FISHER, H. HASHIMOTO and J. W. NEGELE, 79, Sixth International Congress for Electron Microscopy, Kyoto (1966).
3. A. MASCANZONI and G. BAZZICHELLI, *Phil. Mag.* **22** (1970) 857.
4. L. E. MURR, R. J. HORYLEV and W. N. LIN, *ibid* **22** (1970) 515.
5. L. E. MURR, "29th Annual Proc. Electron Microscopy Soc. Amer." (edited by C. J. Arceneaux) (Claitor's, Baton Rouge, 1971) p. 102.
6. R. E. HOOK, *Met. Trans.* **1** (1970) 85.
7. H. GLEITER, E. HORNBOGEN and G. BÄRO, *Acta Metallurgica* **16** (1968) 1053.
8. H. GLEITER, *ibid* **17** (1969) 565.
9. *Idem, Phil. Mag.* **20** (1969) 821.
10. *Idem, Phys. Stat. Sol.* **645** (1971) 9.
11. T. SCHOBER and R. W. BALLUFFI, *ibid* **b44** (1971) 103.
12. *Idem, ibid* **b44** (1971) 115.
13. R. W. BALLUFFI, G. R. WOOLHOUSE and Y. KOMEN, AIME Symposium on the Nature of Grain Boundaries (Plenum Press, New York, 1972) p. 41.
14. R. W. BALLUFFI, Y. KOMEN and T. SCHOBER, *Surface Sci.* **31** (1972) 68.
15. W. BOLLMANN, "Crystal Defects and Crystalline Interfaces" (Springer-Verlag, Berlin, 1970).
16. M. J. MARCINKOWSKI and R. M. POLIAK, *Acta Metallurgica* **12** (1964) 179.
17. M. J. MARCINKOWSKI and HENRY CHESSIN, *Phil. Mag.* **10** (1964) 837.
18. M. J. MARCINKOWSKI, K. SADANANDA and WEN FENG TSENG, *Phys. Stat. Sol.* **17a** (1973) p. 423.
19. J. MARCINKOWSKI and K. SADANANDA, *ibid* **18a** (1973) p. 361.
20. M. J. MARCINKOWSKI, "Fundamental Aspects of Dislocation Theory", NBS Special Publication No. 317, Vol. 1 (edited by John A. Simmons, R. deWit and R. Bullough) (1970) p. 531.
21. M. J. MARCINKOWSKI and WEN FENG TSENG, *Met. Trans.* **1** (1970) 3397.
22. E. S. P. DAS and M. J. MARCINKOWSKI, *J. Mat. Sci. and Eng.* **8** (1971) 189.
23. *Idem, Acta Metallurgica* **20** (1972) 199.
24. M. J. MARCINKOWSKI, "Electron Microscopy and Structure of Materials" (edited by G. Thomas, R. M. Fulrath and R. M. Fisher) (University of California Press, Berkeley, 1972) p. 382.
25. M. J. MARCINKOWSKI and E. S. P. DAS, *Phil. Mag.* **26** (1972) 1281.

26. M. J. MARCINKOWSKI and E. S. DWARAKADASA, *Phys. Stat. Sol.* **19a** (1973).
27. J. C. M. LI, "Electron Microscopy and Strength of Crystals" (edited by G. Thomas and J. Washburn) (Interscience, New York, 1963) p. 713.
28. M. J. MARCINKOWSKI and WEN FENG TSENG, *Met. Trans.* **1** (1970) 3397.
29. P. B. HIRSCH, A. HOWIE, R. B. NICHOLSON, D. W. PASHLEY and M. J. WHELAN, "Electron Microscopy of Thin Crystals" (Butterworth, Washington, D.C., 1965).
30. S. AMELINCKX, "The Direct Observation of Dislocations" (Academic Press, New York, 1964).
31. J. CZERNICHOW, J. P. GUDAS, M. J. MARCINKOWSKI and WEN FENG TSENG, *Met. Trans.* **2** (1971) 2185.
32. M. J. MARCINKOWSKI, "Electron Microscopy and Strength of Crystals" (edited by G. Thomas and J. Washburn) (Interscience, New York, 1963) p. 333.

Received 4 June and accepted 26 July 1973.